Phase variation of ferroelectric $Li_2Sr_{1-x}Ca_x(Nb_{1-x}Ta_x)_2O_7$ by selective reinforcement in the (Nb,Ta)-O covalent bonds

Akitoshi Nakano [1,*] Hirokazu Shirakuni,[1] Takayuki Nagai,[1,†] Yasuhide Mochizuki,[2] Fumiyasu Oba,[2] Hiroko Yokota,[3] Shogo Kawaguchi,[4] Ichiro Terasaki,[1] and Hiroki Taniguchi [1]

[1]*Department of Physics, Nagoya University, Nagoya 464-8602, Japan*
[2]*Laboratory for Materials and Structures, Institute of Innovative Research, Tokyo Institute of Technology, Yokohama 226-8503, Japan*
[3]*Department of Physics, Faculty of Science, Chiba University, 1-33 Yayoi-cho, Inage-ku, Chiba 263-8522, Japan*
[4]*Japan Synchrotron Radiation Research Institute (JASRI), SPring-8, Hyogo 679-5198, Japan*

A phase variation of a pseudo-Roddlesden-Popper-type ferroelectric oxide $Li_2Sr_{1-x}Ca_x(Nb_{1-x}Ta_x)_2O_7$ is systematically investigated using dielectric measurements, second harmonic generation, and x-ray diffraction experiments. We find an exotic *x-T* phase diagram, including paraelectric *Cmcm*, antiferroelectric *Pmcn*, and in-plane antiferroelectric and out-of-plane ferroelectric *P*2₁*cn* phases. At low *x*, we observe large and divergent dielectric anomalies associated with phase transitions from *Cmcm* to *P*2₁*cn*, whereas these become small kinks at high *x*. Structural analyses reveal an internal distortion, and the rotation of octahedra strongly depends on *x*, which is consistent with the lattice dynamics obtained by a density functional theory calculation. These results demonstrate the great tunability of dielectric properties in layered perovskite-type oxides by tuning the chemical bonding state in the octahedron.

I. INTRODUCTION

Ferroelectricity is one of the most intriguing emergent phenomena in condensed matter physics. Perovskite-type oxides, with a chemical formula of the form ABO_3, are some of the most typical ferroelectric materials. The microscopic mechanism of the perovskite-type ferroelectric oxides has been understood as the second-order Jahn-Teller (SOJT) effect, in which the covalency between the *A* or *B* cation and oxygen ions plays a vital role in inducing spontaneous polarization [1–13]. In contrast to this proper ferroelectricity which comes from an electronic origin, the hybrid improper ferroelectricity (HIF) [14,15], the mechanism of which has been understood as the geometrical instabilities of the octahedra network, has recently been proposed in layered perovskite-type oxides. Especially, the Ruddlesden-Popper (RP)-type layered oxides, having a chemical formula of the form $A_3B_2O_7$, have been extensively studied as an ideal platform for HIF [16–20]. Since these two distinct types of ferroelectricity have been developed in the different platforms, the system in which both instabilities compete or cooperate has hardly been investigated. We can expect some exotic dielectric properties in such a system.

In this context, unique ferroelectricity has been reported in an *A*-site ordered pseudo-RP (pRP)-type oxide $Li_2SrNb_2O_7$ (LSNO) [21,22]. This compound shows divergent growth of the dielectric permittivity, which is reminiscent of proper ferroelectricity, ~210 K [21,22]. This is different from ordinary RP-type oxides which show tiny dielectric anomalies associated with the hybrid improper ferroelectric phase transitions [23]. Thus, it is indicated that the SOJT instability plays a vital role in LSNO instead of the geometrical instabilities. Furthermore, LSNO shows a double hysteresis like the polarization-electric field (*P-E*) curve < 100 K, indicating its complex dielectric nature [21,22].

More interestingly, $Li_2CaTa_2O_7$ (LCTO) [24], another isostructural pRP-type compound, shows distinct dielectric properties from LSNO. LCTO shows a tiny dielectric anomaly associated with the phase transition and exhibits a standard ferroelectric *P-E* curve [25]. These features are reminiscent of the HIF [16–20]. The qualitative difference in dielectric properties between isostructural LSNO and LCTO indicates the inherent instability possibly differs between these two systems. The understanding how the microscopic mechanism changes in the isostructural system can provide insight into the field of ferroelectricity.

In this paper, we systematically conducted dielectric measurements and structural analyses on solid solutions $Li_2Sr_{1-x}Ca_x(Nb_{1-x}Ta_x)_2O_7$ (LSCNTO-*x*). We find that the complete solid solution can be formed in this system, and LSCNTO-*x* has a unique phase diagram including paraelectric, antiferroelectric, and ferroelectric phases. We demonstrate that the inherent SOJT and geometrical instability continuously change upon varying *x*. The changing in the atomic orbital component in *B*-O covalent bonding may be a possible route to tune the dielectric responses of the layered perovskite-type oxides.

II. METHODS

The polycrystalline samples of LSCNTO-*x* for *x* = 0, 0.1, 0.2, 0.3, 0.4, 0.5, and 0.6 were prepared by a conventional

---
*nakano.akitoshi@nagoya-u.jp
†Present address: Department of Advanced Materials Science, The University of Tokyo, Kashiwa, Chiba 277-8561, Japan.

solid-state reaction method with powder mixtures of Li_2CO_3 (99.9%), $SrCO_3$ (99.9%), $CaCO_3$ (99.9%), Ta_2O_5(99.99%), and Nb_2O_5 (99.99%), where excess Li_2CO_3 (10% mol) was added to compensate the volatility of Li_2O at high temperatures [21]. For $x = 0.7, 0.8, 0.9$, and 1, the products prepared by the method above included a large amount of impurity phases and showed poor crystallinity due to the short-time and low-temperature sintering condition. Thus, we sintered the pelletized products at 1150°C three times while adding some amount of Li_2CO_3 each time. After that, we loaded the products wrapped in Pt sheets into evacuated tubes and baked them for 6 h. We characterized the obtained powder by x-ray diffraction (XRD) measurements with a wavelength of 0.77 Å using a BL02B2 [26] beamline at SPring-8. The profile-fitting analyses were conducted using JANA2006 [27]. Since samples of $x = 0$–0.4, 0.6, and 1 were strongly influenced by the stacking fault and preferred orientation effects, we calculated the lattice parameters for all LSCNTO-*x* by the LeBail method. We successfully conducted the Rietveld refinement at 100 K for $x = 0.5, 0.7, 0.8$, and 0.9 specimens. We also picked a single crystal for $x = 0$ from the polycrystalline sample and characterized it using BL02B1 [28] beamlines at SPring-8. The crystal-structure analysis was performed by means of a least squares program SHELXL [29]. Dielectric permittivity was measured by using a 4284A precision LCR meter. The second harmonic generation was measured by a reflection mode using an Nd : YVO_4 laser with a wavelength of 1064 nm and a repetition frequency of 2.5 kHz. First-principles calculations used the projector augmented-wave method [30] and the PBEsol functional [31] within the generalized gradient approximation as implemented in VASP [32,33]. The phonon bands were calculated with $2 \times 2 \times 2$ supercells that were constructed from the expansion of the primitive cells using force constants derived from PHONOPY [34,35]. Furthermore, to explore the dynamically stable structure, we set a $\sqrt{2} \times \sqrt{2} \times 1$ supercell of the conventional $I4/mmm$ phase so that the zone-boundary special points $X(\frac{1}{2}, \frac{1}{2}, 0)$ and $M(0, 0, 1)$ are folded into the Γ point. Note that the $I4/mmm$ phase possesses no distortion. Through calculating the phonon band of the supercell, we can derive imaginary phonon modes at X and M points of $I4/mmm$ in the Γ point at once, the method of which was used in the previous studies [36–40]. The calculation of the phonon band is performed until no imaginary phonon mode appears. The chemical bonding analysis through crystal orbital Hamiltonian populations (COHPs) was performed using LOBSTER [41,42].

III. RESULTS AND DISCUSSION

Here, we take a closer look at the crystal structure of the $n = 2$ pRP-type compounds that have a chemical formula of the form $A_2A'B_2O_7$. In the $n = 2$ pRP-type structure, single distorted A_2O and double perovskite-type $A'B_2O_6$ blocks stack in order along the *a*-axis direction. In LSCNTO-*x*, Li, Sr (Ca), and Nb (Ta) occupy the A, A', and B sites, respectively, as shown in Fig. 1(a). Compared with ordinary $n = 2$ RP-type phases, such as $Sr_3Zr_2O_7$, $Ca_3Ti_2O_7$, etc., the interlayer distance between perovskite blocks is shorter by 20% in LSCNTO-*x* because of such distorted Li-O blocks.
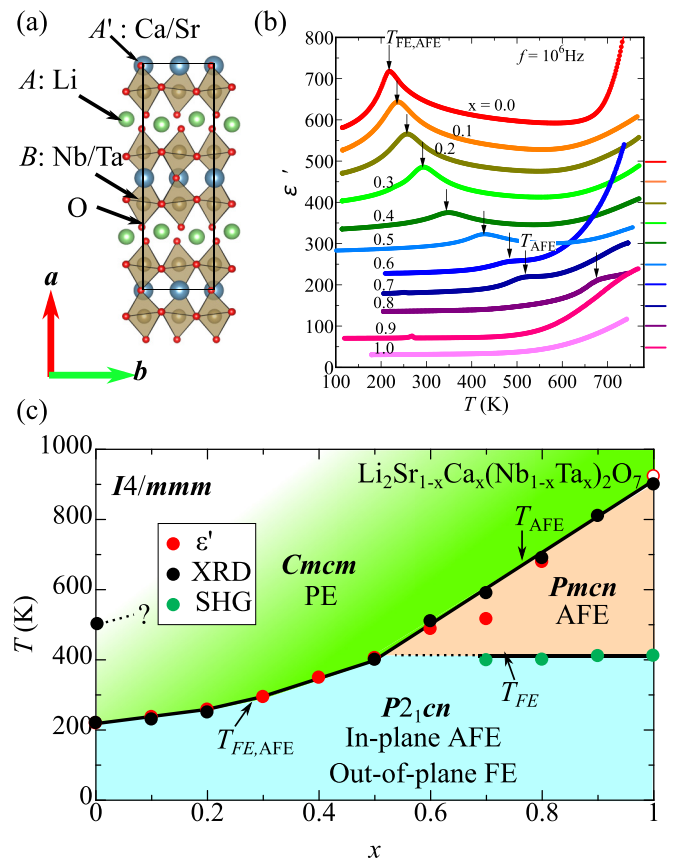

FIG. 1. (a) Crystal structure of $Li_2Sr_{1-x}Ca_x(Nb_{1-x}Ta_x)_2O_7$ viewed from the *c* axis. The structure is visualized using VESTA [43]. (b) Temperature dependence of the dielectric permittivity on various *x*. The zero points of the curves are each shifted in increments of 50 for visibility and are indicated by the color lines by the side of the graph. (c) The phase diagram of $Li_2Sr_{1-x}Ca_x(Nb_{1-x}Ta_x)_2O_7$. The abbreviations of PE, AFE, and FE denote paraelectricity, antiferroelectricity, and ferroelectricity, respectively. The open circle data for $x = 1$ is referred to Ref. [25].

We observe a systematic change in the dielectric responses of LSCNTO-*x*, as shown in Fig. 1(b). LSNO ($x = 0$) shows a diverged dielectric permittivity on the verge of the phase transition ∼217 K. This trend is consistent with previous results [21,22]. When we increase *x*, the peak temperature shifts higher, and the anomaly gradually weakens. This behavior is also consistent with the previous result, where a small anomaly was observed in the paraelectric-to-antiferroelectric phase transition in LCTO ($x = 1$) [25], suggesting a change in the dielectric nature upon chemical substitution.

We summarized the phase diagram of LSCNTO-*x* in Fig. 1(c). Note that the phase diagram is determined by not only the dielectric measurements but also by the temperature-dependent lattice constants and the SHG measurements [44]. In this paper, we focus on three phases in the *x*-*T* diagram: the paraelectric *Cmcm* phase, the antiferroelectric *Pmcn* phase, and the in-plane antiferroelectric and out-of-plane ferroelectric $P2_1cn$ phase. Note that a phase boundary between prototype $I4/mmm$ and *Cmcm* [22] has not been determined yet, although we have confirmed that the *Cmcm* phase continues up to 970 K at $x = 0.5$ [44]. The successive transition

from $Cmcm$ to $P2_1cn$ via $Pmcn$ is consistent with the previous report on LCTO [45]. We define the transition temperatures from $Cmcm$ to $Pmcn$ and from $Pmcn$ to $P2_1cn$ as T_{AFE} and T_{FE}, respectively. We should note that the phase boundaries of the successive phase transitions seem to merge between $x = 0.5$ and 0.6, and we infer the ferroelectric-antiferroelectric-paraelectric triple point, like perovskite-type ferroelectric materials [46], exists in the x-T diagram. At $x < 0.5$, the paraelectric $Cmcm$ phase directly turns to the in-plane antiferroelectric and out-of-plane ferroelectric $P2_1cn$ phase. Thus, we define this transition temperature as $T_{FE,AFE}$.

Here, we should note that the phase assignment for $x = 0$ is different from Ref. [22]. Uppuluri et $al.$ [22] have argued that an in-plane polar $A2_1am$ ($Cmc2_1$ in our setting) phase realizes at room temperature, and an in-plane antipolar $Pnam$ ($Pmcn$) phase realizes at lower temperatures [22]. In addition, the coexistence of $A2_1am$ and $Pnam$ phases was observed between 100 and 250 K [22]. On the other hand, we have previously proposed that a paraelectric $Cmcm$ phase realizes at room temperature, and it changes to an in-plane antiferroelectric and out-of-plane ferroelectric $P2_1cn$ phase < 217 K [21]. The low-temperature ferroelectricity has been confirmed by a small spontaneous polarization in the P-E curve [21]. We should also note that the coexistence of phases has not been observed in our powder XRD [44]. In this paper, we have done the phase assignment based on our previous result. The phase boundaries naturally connect between $x = 0$ and 1 based on our phase assignment for $x = 0$.

The x-T phase diagram for LSCNTO-x is unique in the following points: (i) The cosubstitution effect is weak at low $x(<0.4)$, where $T_{FE,AFE}$ slowly increases with the slope of $dT_{FE,AFE}/dx = 1.5$ K/%. (ii) T_{AFE} rapidly increases with the slope of $dT_{AFE}/dx = 10$ K/% at high $x(>0.5)$. These features are not like those of the single-substituted systems $Li_2Sr(Nb_{1-x}Ta_x)_2O_7$ and $Li_2Sr_{1-x}Ca_xNb_2O_7$. In the case of $Li_2Sr(Nb_{1-x}Ta_x)_2O_7$, $T_{FE,AFE}$ decreases with a linear slope of 6 K/% and completely vanishes at $x = 0.4$ [47]. In the case of $Li_2Sr_{1-x}Ca_xNb_2O_7$, $T_{FE,AFE}$ increases with a slope of 6 K/% until $x = 0.2$ [36]. According to the single-substitution effects, we infer that the slow increase of $T_{FE,AFE}$ at low $x(<0.4)$ stems from the competition between the single Ca- and Ta-substitution effects. However, the rapid increase in T_{AFE} at high $x(>0.5)$ cannot be explained as a competitive picture of individual single-substitution effects like low $x(<0.4)$.

The temperature dependence of the in-plane lattice constants (b and c axes) clearly unveils the qualitative difference between low- and high-x systems. Figures 2(a) and 2(b) show the temperature dependence of the in-plane lattice constants for the $x = 0$ and 1 samples, respectively, obtained by the LeBail fitting assuming the $Pmcn$ space group at all temperatures. For $x = 0$, the in-plane lattice constants b and c correspond within 0.05% between 500 and 1000 K, indicating that the higher symmetry $I4/mmm$ phase exists > 500 K, as previously reported [22]. Below 500 K, the in-plane lattice constants begin to show anisotropy due to out-of-plane tilt of the BO_6 octahedra. Most notably, the in-plane lattice constants increase as temperature decreases below $T_{FE,AFE} \approx 200$ K. This in-plane negative thermal expansion is like that just below the cubic-tetragonal phase transitions of the perovskite-type ferroelectric materials, where the shape of BO_6 octahedra
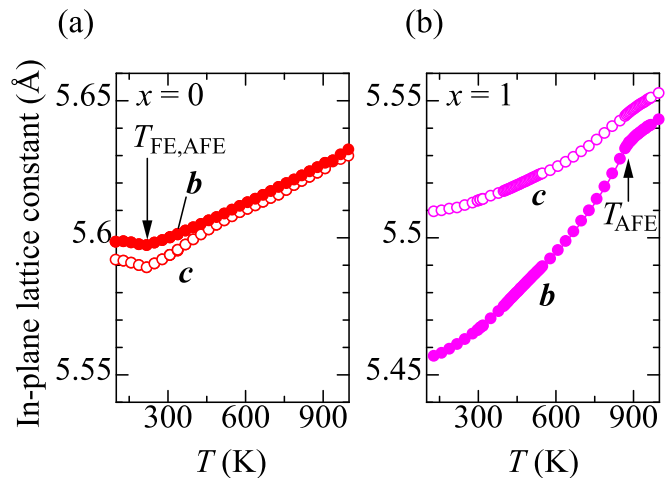

FIG. 2. Temperature dependence of the in-plane lattice constants (b and c) for (a) $x = 0$ and (b) $x = 1$ by the LeBail fitting. In each figure, filled and open circles show the b and c axes, respectively.

become distorted by the strong SOJT effect [48]. We also note that the anisotropy of the in-plane lattice constants $||\mathbf{c}|/|\mathbf{b}| - 1|$ hardly changes between 220 K (0.14%) and 100 K (0.12%).

In contrast, for $x = 1$, the in-plane lattice constants decrease below $T_{AFE} \approx 900$ K, and the in-plane anisotropy is enhanced from 900 K (0.17%) to 100 K (0.90%). This anisotropic shrink of cell parameters has been frequently observed in HIF layered perovskite-type oxides [20], where BO_6 octahedra rotate perpendicularly to the interlayer axis. In addition, we have not observed the phase transition from $Cmcm$ to $I4/mmm$ for $x = 1$ until 1000 K. The temperature dependence of the lattice constants for other x is summarized in Fig. S1 in the Supplemental Material [44].

To elucidate the origin of the unusual phase diagram, we investigate the x dependence of the crystal structure of LSCNTO-x at 100 K. Here, we focus on two distinct structural features: (i) the displacement of the B cation along the c axis, which deforms the BO_6 octahedron, as shown in Fig. 3(a), and (ii) the in-plane lattice anisotropy induced by the rotation of BO_6 octahedra around the a axis, as shown in Fig. 3(b). We can consider that (i) is a measure for the SOJT instability and (ii) is a measure for geometrical instability.

Figure 3(c) shows the x dependence of δl, which is a product of the c-axis length and change in the fractional coordinate of the B cation from the $Cmcm$ phase, at 100 K. Note that we obtained δl by assuming the $Pmcn$ structure to reduce the refinable parameters, although the actual space group of LSCNTO-x at 100 K is $P2_1cn$ [49]. Here, δl reaches ~ 0.1 Å for $x = 0$, when we use the parameters $c = 5.5982$ Å and the change in the fractional coordinate of 0.01696 (see Table S1 in the Supplemental Material [44] and table S2 of Ref. [21]). This value is comparable with that of Ti ions in $BaTiO_3$, which is associated with the cubic-to-tetragonal transition. On the other hand, the in-plane lattice anisotropy $||\mathbf{c}|/|\mathbf{b}| - 1|$ in Fig. 3(c) is very small due to the small rotation of NbO_6 octahedra. This indicates that the SOJT instability dominates the phase transition in early LSCNTO-x. Here, δl decreases upon
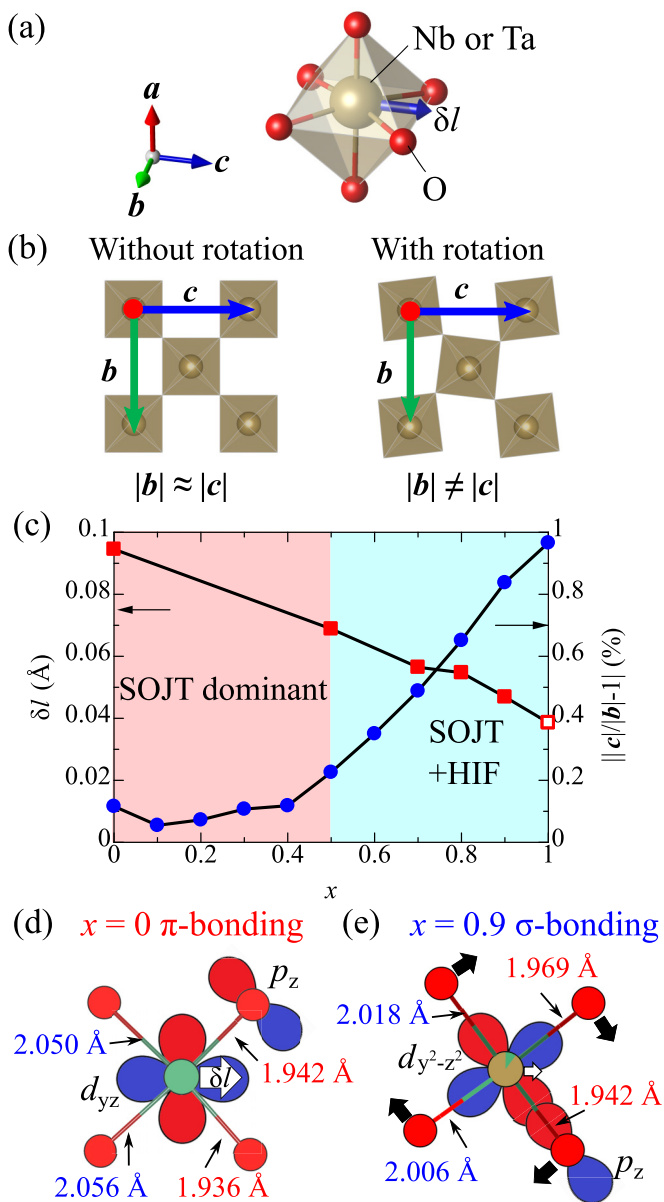
FIG. 3. Schematics of (a) the displacement of the B cation in an octahedron, (b) the in-plane lattice anisotropy induced by the octahedra rotation. The blue vector in (a) shows the B-cation displacement along the c axis (δl). (c) The x dependence of δl and lattice anisotropy at 100 K. The open square data for $x = 1$ is evaluated from room temperature data of tables 1 and 2 in Ref. [24] (the two Ta sites are averaged). Schematics of the (d) π bonding and (e) σ bonding in a BO_6 octahedron. The analyzed bond lengths between the B cation and oxygen are also shown for $x = 0$ and 0.9.

increasing x, indicating the weakening of the SOJT instability. Instead, the in-plane lattice anisotropy rapidly increases above $x = 0.4$, indicating the enhancement of the rotation of the BO_6 octahedra induced by the geometrical instability.

Interestingly, the small but finite δl exists at $x = 0.7$, 0.8, 0.9, and 1 [45]. This is in contrast to the result of Li$_2$Sr(Nb$_{1-x}$Ta$_x$)$_2$O$_7$, where δl vanishes at $x = 0.4$ as a result of the complete disappearance of the SOJT instability [47]. This indicates that, when we vary x of LSCNTO-$x > 0.4$,

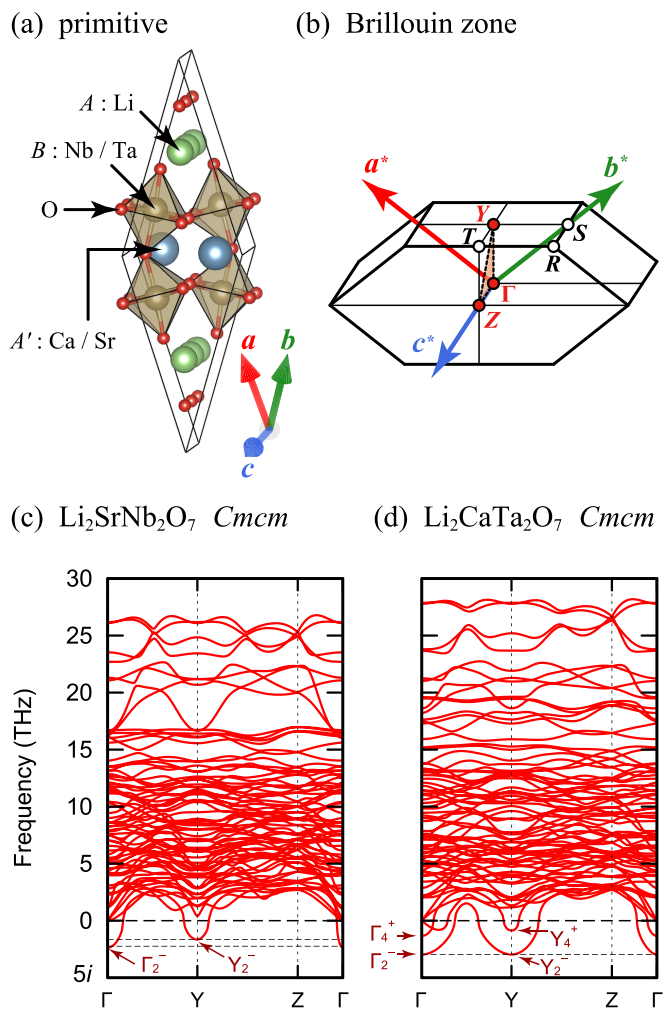FIG. 4. (a) Primitive cell of the *Cmcm* phase for Li$_2$$A'$$B_2O_7$, which is derived from the first-principles calculations. The structure is visualized with VESTA [43]. (b) The Brillouin zone of base-centered orthorhombic Bravais lattice, which includes the space group *Cmcm* [50]. The red, green, and blue axes, respectively, indicate the reciprocal lattice vectors a^*, b^*, and c^* in the *Cmcm* primitive cell. The broken line shows the band path used in the phonon band calculation. Calculated phonon band structures of (c) Li$_2$SrNb$_2$O$_7$ [36,47] and (d) Li$_2$CaTa$_2$O$_7$ in the paraelectric *Cmcm* phases. Frequencies less than zero have imaginary units. Irreducible representations with imaginary frequency are also indicated.

there is not a simple crossover of the transition mechanism from the SOJT to geometrical instability. As described below, the SOJT effect survives in the strongly rotated BO_6 octahedra with the change in the chemical bonding nature at high x compositions.

Figures 3(d) and 3(e) schematically shows the analytical in-plane bond lengths of the BO_6 octahedra for $x = 0$ and 0.9, respectively. For $x = 0$, δl is large, whereas the rotation is very small, resulting in an almost isotropic decrease in two Nb-O bonds by 5%. This trend is understood by means of the enhanced covalency of the π-bonding orbital, which consists of Nb-4d_{yz} and O-2p_z orbitals, as shown in Figs. 3(d) and S6(e) in the Supplemental Material [44,47]. On the other hand, for $x = 0.9$, the combination of the SOJT and

geometrical instability leads to an anisotropic decrease in B-O bonds; the difference between the shortest and longest is ~4%, and that between the second shortest and longest is ~2%, which are consistent with the calculation results [44]. This situation has been recently predicted in $Li_2CaNb_2O_7$ [36], where the σ bonding, which consists of Nb-$4d_{y_{2-z^2}}$ and O-$2p_z$, is reinforced to give rise to a global energy lowering, as shown in Fig. 3(e). This trend is also confirmed for LCTO by the COHP analysis (Fig. S6 in the Supplemental Material [44]).

We infer the bonding orbital, which drives the phase transition, switches from π to σ bonding above $x = 0.4$ since the lattice anisotropy $||\mathbf{c}|/|\mathbf{b}| - 1|$ starts to increase at that x. The rapid increase of dT_{AFE}/dT at high $x(>0.5)$ must be related to this switching. We also deduce that the switching of the bonding nature gives rise to the emergence of the antiferroelectric phase above $x = 0.5$.

Let us discuss the phase transitions in LSNO and LCTO from the viewpoint of the lattice dynamics. Figures 4(a) and 4(b) respectively show the primitive cell and Brillouin zone of the $Cmcm$ phase. In this setting, the zone-boundary special points of Y and Z are defined, respectively, as $(\frac{1}{2}, \frac{1}{2}, 0)$ and $(0, 0, \frac{1}{2})$, which can be represented as $\frac{1}{2}\mathbf{a}^* + \frac{1}{2}\mathbf{b}^*$, and $\frac{1}{2}\mathbf{c}^*$ [44]. The band dispersions, which are shown in Figs. 4(c) and 4(d), are calculated along the path of Γ-Y-Z-Γ.

For LSNO [Fig. 4(c)], an imaginary Γ_2^- mode is the most unstable. This indicates a potential soft phonon mode at the Γ point which results in proper ferroelectricity [51–53]. Although the freezing of the Y_2^- mode has been experimentally confirmed in LSNO [21], the divergent growth of the dielectric permittivity around $T_{FE,AFE}$ at low $x(<0.4)$ may stem from the softening of the Γ mode. On the other hand, for LCTO [Fig. 4(d)], the imaginary frequency of the zone-boundary Y_2^- mode becomes as large as that of the Γ_2^- mode. The weakening of the dielectric anomalies around T_{AFE} at high $x(>0.5)$ may come from the hardening of the Γ_2^- soft mode relative to the Y_2^- mode. Since the direction of Γ-Y corresponds to the $a + b$ direction in the primitive cell (a-axis direction of the conventional cell), the Y_2^- soft mode can generate the antiparallel displacement of the B cation and out-of-phase oc-

tahedral rotations between stacking double-perovskite layers. Theoretically derived stable structures by freezing Y_2^- modes of LSNO and LCTO strongly support our structural analyses; the displacement of Nb in LSNO is larger than Ta in LCTO, whereas the rotation of the NbO_6 octahedron in LSNO is much smaller than the TaO_6 octahedron in LCTO [44].

This result clearly shows that LSCNTO-x is a very useful playground to control the ferroelectricity through tuning two types of the instabilities in the identical crystal structure. This dual tunability has not been considered in the typical perovskite-type and RP-type oxides thus far. We infer that the short interlayer distance and asymmetric crystal field of the BO_6 octahedra play a role in rendering the intermediate dielectric and phase transition properties between perovskite-type and layered perovskite-type oxides to pRP phases.

IV. SUMMARY

In summary, we revealed an intriguing x-T phase diagram for $Li_2Sr_{1-x}Ca_x(Nb_{1-x}Ta_x)_2O_7$ (LSCNTO-x). At low $x(<0.4)$, the SOJT effect mainly drives the phase transition, whereas at high $x(>0.5)$, geometrical instability becomes effective. We have revealed that the steep enhancement of the transition temperature above $x = 0.5$ stems from the cooperative mechanism of the SOJT effect and geometrical instability. We propose that LSCNTO-x is a useful playground to investigate the relationship between structures, electronic states, and functionalities in layered perovskite ferroelectric materials.

[1] R. G. Pearson, A symmetry rule for predicting molecular structures, J. Am. Chem. Soc. **91**, 4947 (1969).

[2] R. G. Pearson, The second-order Jahn-Teller effect, J. Mol. Struct.: THEOCHEM **103**, 25 (1983).

[3] T. Hughbanks, Superdegenerate electronic energy levels in extended structures, J. Am. Chem. Soc. **107**, 6851 (1985).

[4] R. A. Wheeler, M. H. Whangbo, T. Hughbanks, R. Hoffmann, J. K. Burdett, and T. A. Albright, Symmetric vs. asymmetric linear M-X-M linkages in molecules, polymers, and extended networks, J. Am. Chem. Soc. **108**, 2222 (1986).

[5] R. E. Cohen, Origin of ferroelectricity in perovskite oxides, Nature (London) **358**, 136 (1992).

[6] M. Posternak, R. Resta, and A. Baldereschi, Role of covalent bonding in the polarization of perovskite oxides: the case of $KNbO_3$, Phys. Rev. B **50**, 8911 (1994).

[7] M. Kunz and I. D. Brown, Out-of-center distortions around octahedrally coordinated d^0 transition metals, J. Solid State Chem. **115**, 395 (1995).

[8] J. B. Goodenough, Jahn-Teller phenomena in solids, Annu. Rev. Mater. Sci. **28**, 1 (1998).

[9] Y. Kuroiwa, S. Aoyagi, A. Sawada, J. Harada, E. Nishibori, M. Takata, and M. Sakata, Evidence for Pb-O Covalency in Tetragonal $PbTiO_3$, Phys. Rev. Lett. **87**, 217601 (2001).

[10] H. Taniguchi, H. P. Soon, T. Shimizu, H. Moriwake, Y. J. Shan, and M. Itoh, Mechanism for suppression of ferroelectricity in $Cd_{1-x}Ca_xTiO_3$, Phys. Rev. B **84**, 174106 (2011).

[11] H. Moriwake, A. Kuwabara, C. A. J. Fisher, H. Taniguchi, M. Itoh, and I. Tanaka, First-principles calculations of lattice dynamics in $CdTiO_3$ and $CaTiO_3$: phase stability and ferroelectricity, Phys. Rev. B **84**, 104114 (2011).

[12] H. Taniguchi, H. P. Soon, H. Moriwake, Y. J. Shan, and M. Itoh, Effect of Ca-substitution on $CdTiO_3$ studied by Raman scattering and first principles calculations, Ferroelectrics **426**, 268 (2012).

[13] I. B. Bersuker, Pseudo Jahn-Teller Origin of Perovskite Multiferroics, Magnetic-Ferroelectric Crossover, and Magneto-electric Effects: The $d^0 - d^{10}$ Problem, Phys. Rev. Lett. **108**, 137202 (2012).

[14] N. A. Benedek and C. J. Fennie, Hybrid Improper Ferroelectricity: A Mechanism for Controllable Polarization-Magnetization Coupling, Phys. Rev. Lett. **106**, 107204 (2011).

[15] N. A. Benedek, A. T. Mulder, and C. J. Fennie, Polar octahedral rotations: a path to new multifunctional materials, J. Solid State Chem. **195**, 11 (2012).

[16] Y. S. Oh, X. Luo, F.-T. Huang, Y. Wang, and S.-W. Cheong, Experimental demonstration of hybrid improper ferroelectricity and the presence of abundant charged walls in $(Ca, Sr)_3Ti_2O_7$ crystals, Nat. Mater. **14**, 407 (2015).

[17] X. Q. Liu, B. H. Chen, J. J. Lu, Z. Z. Hu, and X. M. Chen, Hybrid improper ferroelectricity in B-site substituted $Ca_3Ti_2O_7$: the role of tolerance factor, Appl. Phys. Lett. **113**, 242904 (2018).

[18] S. Yoshida, K. Fujita, H. Akamatsu, O. Hernandez, A. Sen Gupta, F. G. Brown, H. Padmanabhan, A. S. Gibbs, T. Kuge, R. Tsuji, S. Murai, J. M. Rondinelli, V. Gopalan, and K. Tanaka, Ferroelectric $Sr_3Zr_2O_7$: competition between hybrid improper ferroelectric and antiferroelectric mechanisms, Adv. Funct. Mater. **28**, 1801856 (2018).

[19] Y. Wang, F. T. Huang, X. Luo, B. Gao, and S. W. Cheong, The first room-temperature ferroelectric Sn insulator and its polarization switching kinetics, Adv. Mater. **29**, 1601288 (2017).

[20] S. Yoshida, H. Akamatsu, R. Tsuji, O. Hernandez, H. Padmanabhan, A. Sen Gupta, A. S. Gibbs, K. Mibu, S. Murai, J. M. Rondinelli, V. Gopalan, K. Tanaka, and K. Fujita, Hybrid improper ferroelectricity in $(Sr, Ca)_3Sn_2O_7$ and beyond: universal relationship between ferroelectric transition temperature and tolerance factor in $n = 2$ Ruddlesden-Popper phases, J. Am. Chem. Soc. **140**, 15690 (2018).

[21] T. Nagai, H. Shirakuni, A. Nakano, H. Sawa, H. Moriwake, I. Terasaki, and H. Taniguchi, Weak ferroelectricity in $n = 2$ pseudo Ruddlesden-Popper-type niobate $Li_2SrNb_2O_7$, Chem. Mater. **31**, 6257 (2019).

[22] R. Uppuluri, H. Akamatsu, A. Sen Gupta, H. Wang, C. M. Brown, K. E. Agueda Lopez, N. Alem, V. Gopalan, and T. E. Mallouk, Competing polar and antipolar structures in the Ruddlesden-Popper layered perovskite $Li_2SrNb_2O_7$, Chem. Mater. **31**, 4418 (2019).

[23] B. H. Chen, T. L. Sun, X. Q. Liu, X. L. Zhu, H. Tian, and X. M. Chen, Enhanced hybrid improper ferroelectricity in $Sr_{3-x}Ba_xSn_2O_7$ ceramics with a Ruddlesden-Popper (R-P) structure, Appl. Phys. Lett. **116**, 042903 (2020).

[24] Z. Liang, K. Tang, Q. Shao, G. Li, S. Zeng, and H. Zheng, Synthesis, crystal structure, and photocatalytic activity of a new two-layer Ruddlesden-Popper phase, $Li_2CaTa_2O_7$, J. Solid State Chem. **181**, 964 (2008).

[25] B. H. Zhang, Z. Z. Hu, B. H. Chen, X. Q. Liu, and X. M. Chen, Room-temperature ferroelectricity in A-site ordered Ruddlesden-Popper $Li_2CaTa_2O_7$ ceramics, J. Materiomics **6**, 593 (2020).

[26] S. Kawaguchi, M. Takemoto, K. Osaka, E. Nishibori, C. Moriyoshi, Y. Kubota, Y. Kuroiwa, and K. Sugimoto, High-throughput powder diffraction measurement system consisting of multiple MYTHEN detectors at beamline BL02B2 of SPring-8, Rev. Sci. Instrum. **88**, 085111 (2017).

[27] V. Petricek, M. Dusek, and L. Palatinus, Crystallographic computing system JANA2006: general features, Z. Kristallogr. **229**, 345 (2014).

[28] L. Krause, K. Tolborg, T. B. E. Gronbech, K. Sugimoto, B. B. Inverson, and J. Overgaard, Accurate high-resolution single-crystal diffraction data from a Pilatus3 X CdTe detector, J. Appl. Cryst. **53**, 635 (2020).

[29] G. M. Sheldrick, Crystal structure refinement with SHELXL, Acta Cryst. **C71**, 3 (2015).

[30] P. E. Blöchl, Projector augmented-wave method, Phys. Rev. B **50**, 17953 (1994).

[31] J. P. Perdew, A. Ruzsinszky, G. I. Csonka, O. A. Vydrov, G. E. Scuseria, L. A. Constantin, X. Zhou, and K. Burke, Restoring the Density-Gradient Expansion for Exchange in Solids and Surfaces, Phys. Rev. Lett. **100**, 136406 (2008).

[32] G. Kresse and J. Furthmüller, Efficient iterative schemes for *ab initio* total-energy calculations using a plane-wave basis set, Phys. Rev. B **54**, 11169 (1996).

[33] G. Kresse and D. Joubert, From ultrasoft pseudopotentials to the projector augmented-wave method, Phys. Rev. B **59**, 1758 (1999).

[34] A. Togo and I. Tanaka, First principles phonon calculations in materials science, Scr. Mater. **108**, 1 (2015).

[35] A. Togo, F. Oba, and I. Tanaka, Transition pathway of CO_2 crystals under high pressures, Phys. Rev. B **77**, 184101 (2008).

[36] Y. Mochizuki, T. Nagai, H. shirakuni, A. Nakano, F. Oba, I. Terasaki, and H. Taniguchi, Coexisting mechanisms for the ferroelectric phase transition in $Li_2SrNb_2O_7$, Chem. Mater. **33**, 1257 (2021).

[37] H. Akamatsu, K. Fujita, T. Kuge, A. S. Gupta, A. Togo, S. Lei, F. Xue, G. Stone, J. M. Rondinelli, L. Chen, I. Tanaka, V. Gopalan, and K. Tanaka, Inversion Symmetry Breaking by Oxygen Octahedral Rotations in the Ruddlesden-Popper $NaRTiO_4$ Family, Phys. Rev. Lett. **112**, 187602 (2014).

[38] Y. Mochizuki, H. Akamatsu, Y. Kumagai, and F. Oba, Strain-engineered Peierls instability in layered perovskite $La_3Ni_2O_7$ from first principles, Phys. Rev. Materials **2**, 125001 (2018).

[39] Y. Mochizuki, Y. Kumagai, H. Akamatsu, and F. Oba, Polar metallic behavior of strained antiperovskites $ACNi_3$ (A = Mg, Zn, and Cd) from first principles, Phys. Rev. Materials **2**, 125004 (2018).

[40] Y. Mochizuki, H. Sung, A. Takahashi, Y. Kumagai, and F. Oba, Theoretical exploration of mixed-anion antiperovskite semiconductors M_3XN (M = Mg, Ca, Sr, Ba; X = P, As, Sb, Bi), Phys. Rev. Materials **4**, 044601 (2020).

[41] R. Dronskowski and P. E. Blöchl, Crystal orbital Hamilton populations (COHP): energy-resolved visualization of chemical bonding in solids based on density-functional calculations, J. Phys. Chem. **97**, 8617 (1993).

[42] S. Maintz, V. L. Deringer, A. L. Tchougreeff, and R. Dronskowski, LOBSTER: a tool to extract chemical bonding from plane-wave based DFT, J. Comput. Chem. **37**, 1030 (2016).

[43] F. Izumi and K. Momma, Three-dimensional visualization in powder diffraction, Solid State Phenom. **130**, 15 (2007).

[44] See Supplemental Material at http://link.aps.org/supplemental/10.1103/PhysRevMaterials.6.044412 for the temperature-dependent lattice constants and the SHG measurements, the temperature-dependent superlattice intensity of LSCNTO-0.5, the temperature-dependent superlattice intensity of LSNO, the COHPs analysis for LCTO, the crystallographic table for LSNO, and the relaxed octahedral geometry of LCTO.

[45] C. G. Galven, D. Mounier, B. Bouchevreau, E. Suard, A. Bulou, M. Lopez, and F. L. Berre, Phase transitions in the Ruddlesden-Popper phase $Li_2CaTa_2O_7$: x-ray and neutron powder thermodiffraction, TEM, Raman, and SHG experiments, Inorg. Chem. **55**, 2309 (2016).

[46] V. M. Ishchuk and V. L. Sobolev, Investigation of two-phase nucleation in paraelectric phase of ferroelectrics with ferroelectric-antiferroelectric-paraelectric triple point, J. Appl. Phys. **92**, 2086 (2002).

[47] T. Nagai, Y. Mochizuki, H. Shirakuni, A. Nakano, F. Oba, I. Terasaki, and H. Taniguchi, Phase transition from weak ferroelectricity to incipient ferroelectricity in $Li_2Sr(Nb_{1-x}Ta_x)_2O_7$, Chem. Mater. **32**, 744 (2020).

[48] J. S. O. Evans, Negative thermal expansion materials, J. Chem. Soc., Dalton Trans. **1999**, 3317 (1999).

[49] We used space group *Pmcn* for the structural optimization to reduce refinable parameters, although the actual space group of LSCNTO-*x* at 100 K is $P2_1cn$. There are two inequivalent BO_6 octahedral sites in $P2_1cn$, whereas there is only one BO_6 octahedral site in *Pmcn*. In the present analyses, we can obtain average δl for the two octahedral sites of LSCNTO-*x* at 100 K by assuming the *Pmcn* structure.

[50] M. I. Aroyo, D. Orobengoa, G. de la Flor, E. S. Tasci, J. M. Perez-Mato, and H. Wondratschek, Brillouin-zone database on the Bilbao Crystallographic Server, Acta Cryst. A **70**, 126 (2014).

[51] W. Cochran, Crystal stability and the theory of ferroelectricity, Adv. Phys. **9**, 387 (1960).

[52] W. Cochran, Crystal stability and the theory of ferroelectricity part II. Piezoelectric crystals, Adv. Phys. **10**, 401 (1961).

[53] J. F. Scott, Soft-mode spectroscopy: experimental studies of structural phase transitions, Rev. Mod. Phys. **46**, 83 (1974).